

Density Imaging Using a Multiple-Frequency DBIM Approach

Roberto Lavarello, *Member, IEEE* and Michael Oelze, *Senior Member, IEEE*

Abstract—Current inverse scattering methods for quantitative density imaging have limitations that keep them from practical experimental implementations. In this work, an improved approach, termed the multiple-frequency distorted Born iterative method (MF-DBIM) algorithm, was developed for imaging density variations. The MF-DBIM approach consists of inverting the wave equation by solving for a single function that depends on both sound speed and density variations at multiple frequencies. Density information was isolated by using a linear combination of the reconstructed single-frequency profiles. Reconstructions of targets using MF-DBIM from simulated data were compared with reconstructions using methods currently available in the literature, i.e., the dual-frequency DBIM (DF-DBIM) and T-matrix approaches. Useful density reconstructions, i.e., root mean square errors (RMSEs) less than 30%, were obtained with MF-DBIM even with 2% Gaussian noise in the simulated data and using frequency ranges spanning less than an order of magnitude. Therefore, the MF-DBIM approach outperformed both the DF-DBIM method (which has problems converging with noise even an order of magnitude smaller) and the T-matrix method (which requires a ka factor close to unity to achieve convergence). However, the convergence of all the density imaging algorithms was compromised when imaging targets with object functions exhibiting high spatial frequency content.

I. INTRODUCTION

THE quantitative estimation and imaging of structural and acoustic parameters using ultrasound have been extensively studied for many years as tools for tissue characterization. Several techniques with different levels of computational complexity have been explored, including ultrasonic envelope analysis [1], [2], quantitative ultrasound techniques based on backscattered data [3]–[6], quantitative elastographic techniques [7]–[9], and acoustic microscopy [10]–[12].

Acoustic tomography is a quantitative imaging technique that aims to reconstruct material properties based on scattered pressure measurements. Typically, density changes are neglected to obtain estimates of speed of sound and attenuation [13]–[15]. However, experimental evidence is available in the literature suggesting that relative density changes in tissues may be comparable in mag-

nitude to relative sound speed changes [16], [17]. Although there exists information that suggests density and speed of sound are highly correlated in benign tissues [18], actual values of density and compressibility are not known for many disease states. Sound speed and density values reported by Saijo *et al.* [19] for three different myocardial tissue types suggested that although density seemed to increase with increasing sound speed, the relationship between the corresponding sound speed and density contrasts (relative to water) was not linear. For the case of breast tissue, Yang *et al.* [20] stated that even though density was observed to generally increase with increasing speed of sound, this was not the case when considerable fibrous tissue was mingled with fatty tissue. Some studies available in the literature [21], [22] suggest density variations may play an important role in scattering from tissues. Therefore, determining density distributions may provide additional information or contrast in imaging for cancer detection.

Some studies of density imaging based on single-scattering formulations are available in the literature [23]–[27]. Inverse scattering methods, which take into account multiple scattering, have also been studied. These methods can be roughly classified into two categories. The first approach consists of inverting the wave equation by solving for a single function that depends on both speed of sound and density variations, and using data at two frequencies to isolate density information [28], [29]. The second approach consists of solving the wave equation for two functions simultaneously: one that depends only on compressibility and one that depends only on density variations [30]–[32]. It has been previously reported in the literature that both approaches have limitations that keep them from practical experimental implementations [33], [34]. In particular, the first approach (as exemplified by the dual-frequency distorted Born iterative method, DF-DBIM) was found to be very sensitive to the termination tolerance of the single-frequency reconstructions, and the second approach (as exemplified by the T-matrix approach) was found to require a very large bandwidth.

The remainder of this work is devoted to the derivation and assessment of a variation of the DF-DBIM approach, termed here the multiple-frequency distorted Born iterative method (MF-DBIM) approach. In this work, several aspects of the proposed algorithm were explored, including the effects of density and speed of sound contrasts, sensitivity to noise, and the effects of algorithmic variables such as the bandwidth and the separation among frequencies used in the inversion.

Manuscript received January 2, 2010; accepted July 22, 2010. This work was supported in part by a grant from the 3M Corporation.

The authors are with the Department of Electrical and Computer Engineering, University of Illinois at Urbana-Champaign, Urbana, IL (e-mail: lavarell@uiuc.edu).

R. Lavarello is also with the Sección Electricidad y Electrónica, Departamento de Ingeniería, Pontificia Universidad Católica del Perú, Lima, Perú.

Digital Object Identifier 10.1109/TUFFC.2010.1713

II. METHODS

A. Variable Density and the Distorted Born Iterative Method

The details of the distorted Born iterative method (DBIM) [35]–[37] in the presence of density variations are presented here for completeness. The wave propagation in an inhomogeneous medium is described by [38]

$$\rho(\vec{r})\nabla \cdot [\rho^{-1}(\vec{r})\nabla p(\vec{r})] + k^2(\vec{r})p(\vec{r}) = -\phi^{\text{inc}}(\vec{r}), \quad (1)$$

where $p(\vec{r})$ is the acoustical pressure, $\phi^{\text{inc}}(\vec{r})$ is the acoustic source, and $k(\vec{r})$ and $\rho(\vec{r})$ are the wave number and density distributions, respectively. By applying the change of variables $p(\vec{r}) = f(\vec{r})\rho^{1/2}(\vec{r})$ [39], [40], (1) can be rewritten in integral form as

$$p(\vec{r}) = e_s(\vec{r}) + \int_{\Omega} d\vec{r}' \mathcal{O}(\vec{r}', \omega) p(\vec{r}') G_0(\vec{r}, \vec{r}'), \quad (2)$$

where $e_s(\vec{r})$ is the incident field caused by a source located at \vec{r}_s , $s = 0, 1, \dots, N_s$, and $G_0(\vec{r}, \vec{r}')$ is the Green's function in a homogeneous background with wave number k_0 . Assuming the speed of sound $c(\vec{r})$ is weakly dispersive and neglecting attenuation for simplicity, the object function \mathcal{O} is given by

$$\begin{aligned} \mathcal{O}(\vec{r}, \omega) &= (k^2(\vec{r}) - k_0^2) - \rho^{1/2}(\vec{r})\nabla^2 \rho^{-1/2}(\vec{r}) \\ &= \left[\frac{\omega^2}{c^2(\vec{r})} - \frac{\omega^2}{c_0^2} \right] - \rho^{1/2}(\vec{r})\nabla^2 \rho^{-1/2}(\vec{r}), \end{aligned} \quad (3)$$

where ω is the angular frequency of the incident harmonic wave and c_0 is the sound speed in the background. The integral equation can be used to solve both for the pressure field inside the computational domain \bar{p} and the scattered field outside the computational domain \bar{p}^{sc} . The DBIM is a Newton-type algorithm that obtains an estimate of the function $\mathcal{O}(\vec{r}, \omega)$ using (2) and measurements of the scattered field $p^{\text{sc}}(\vec{r}) = p(\vec{r}) - e_s(\vec{r})$ caused by the imaging target. In this work, (2) was discretized using sinc-based functions and delta testing functions [41]. A trial $\bar{\mathcal{O}}_{(0)}$ is chosen for which the corresponding scattered field is calculated. Next, the object function is updated as $\bar{\mathcal{O}}_{(n+1)} = \bar{\mathcal{O}}_{(n)} + \Delta\bar{\mathcal{O}}_{(n)}$, where $\Delta\bar{\mathcal{O}}_{(n)}$ is given by the regularized optimization problem

$$\Delta\bar{\mathcal{O}}_{(n)} = \underset{\Delta\mathcal{O}}{\text{argmin}} \|\Delta\bar{p}^{\text{sc}} - \bar{F}_{(n)} \cdot \Delta\mathcal{O}\|_2^2 + \gamma \|\Delta\mathcal{O}\|_2^2, \quad (4)$$

where $\Delta\bar{p}^{\text{sc}}$ contains the difference between the predicted and measured scattered fields, γ is the regularization parameter, and $\bar{F}_{(n)}$ is the so-called Frechet derivative matrix [36]. The iterative process is repeated until the relative residual error (RRE), given by $\text{RRE} = \|\Delta\bar{p}^{\text{sc}}\|_2 / \|\bar{p}^{\text{sc}}\|_2$, falls within a desired termination tolerance $t\%$.

B. The Multiple-Frequency DBIM (MF-DBIM) Algorithm

To estimate density profiles, one can exploit the fact that the term in brackets in (3) scales with ω^2 whereas the second term $\mathcal{F}_\rho = \rho^{1/2}(\vec{r})\nabla^2 \rho^{-1/2}(\vec{r})$ is frequency independent. Therefore, multiple frequency information allows isolating \mathcal{F}_ρ , after which density images can be constructed by solving the differential equation

$$\begin{aligned} \nabla^2 u(\vec{r}) - \mathcal{F}_\rho(\vec{r})u(\vec{r}) &= \mathcal{F}_\rho(\vec{r}), \quad \vec{r} \in \Omega \\ u(\vec{r}) &= 0, \quad \vec{r} \notin \Omega, \end{aligned} \quad (5)$$

where $u(\vec{r}) = (\rho_r^{-1/2}(\vec{r}) - 1)$. In this study, (5) was solved by converting it to the matrix equation

$$\begin{aligned} \bar{G} \cdot \bar{u} &= \bar{F}_\rho \\ \bar{G} &= (\mathcal{L} - \mathcal{D}(\bar{F}_\rho)), \end{aligned} \quad (6)$$

where \bar{u} is a vector with the values of $u(\vec{r})$, \bar{F}_ρ is a vector with the values of $\mathcal{F}_\rho(\vec{r})$, \mathcal{L} is a matrix approximation of the ∇^2 operator using a finite difference template, and \mathcal{D} is an operator that transforms a vector into a diagonal matrix.

A minimum of two estimates of $\mathcal{O}(\vec{r}, \omega_i)$ at two different frequencies are required to separate speed of sound and density information. In general, if a set of reconstructions $\mathcal{O}_i = \mathcal{O}(\vec{r}, \omega_i)$ at frequencies ω_i , $i = 1, 2, \dots, N_f$ are available, the least mean squares estimator

$$\begin{aligned} \mathcal{F}_\rho(\vec{r}) &= \frac{\left(\sum_{i=1}^{N_f} \omega_i^2 \right) \left(\sum_{i=1}^{N_f} \omega_i^2 \mathcal{O}_i(\vec{r}) \right) - \left(\sum_{i=1}^{N_f} \omega_i^4 \right) \left(\sum_{i=1}^{N_f} \mathcal{O}_i(\vec{r}) \right)}{N_f \sum_{i=1}^{N_f} \omega_i^4 - \left(\sum_{i=1}^{N_f} \omega_i^2 \right)^2} \end{aligned} \quad (7)$$

allows for the isolation of density contributions to the object function. $\mathcal{F}(\vec{r})$ profiles were estimated by combining $\mathcal{O}(\vec{r}, \omega)$ profiles obtained at frequencies between f_{min} and f_{max} in steps of Δf , where the frequency increment Δf is given by

$$\Delta f = \frac{f_{\text{max}} - f_{\text{min}}}{N_f - 1}. \quad (8)$$

The quality of the density reconstructions when using (7) is compromised by improper cancellation of the speed-of-sound components of the reconstructed \mathcal{O}_i . This effect is exacerbated when large termination tolerance values are used, which reduces the correlation among the speed-of-sound components at different frequencies. Here it is hypothesized that frequency hopping [42], [43], i.e., the use of lower frequency reconstructions as initial guesses for higher frequency reconstructions, may im-

prove on the speed-of-sound term cancellation and therefore improve on the quality of tomographic density imaging. When performing the reconstruction using data corresponding to frequency ω_i , the most accurate available initial guess is

$$\mathcal{O}^{(0)}(\vec{r}, \omega_i) = \left(\frac{\omega_{i-1}}{\omega_i} \right)^2 \mathcal{O}(\vec{r}, \omega_{i-1}), \quad (9)$$

where $\mathcal{O}(\vec{r}, \omega_{i-1})$ is the final reconstruction obtained at the nearest lower frequency ω_{i-1} . However, if ω_{i-1} and ω_i are too close to each other, no iterations will occur when processing the data at frequency ω_i for a given termination tolerance. On the other hand, if the initial guess is too far away from the true profile, correlation will be lost between $\mathcal{O}_{i-1}(\vec{r})$ and $\mathcal{O}_i(\vec{r})$. Therefore, the initial guess when processing the i th frequency was chosen as

$$\mathcal{O}_{\text{MF-DBIM}}^{(0)}(\vec{r}, \omega_i) = \beta \mathcal{O}^{(0)}(\vec{r}, \omega_i), \quad (10)$$

where β is a contraction factor. In this work the contraction factor was chosen as $\beta = (1 - 1.5t\%)$, where $t\%$ is the termination tolerance. This choice of β was empirically determined to be appropriate for making DBIM iterate at least one time when low Δf values were used. A conventional 2-D median filter of size 3 by 3 pixels was used to smooth $\mathcal{O}_{\text{MF-DBIM}}^{(0)}(\vec{r}, \omega_i)$.

Frequency hopping improves on the correlation among all profiles except the one obtained at frequency f_{\min} , which is obtained using an all-zero initial guess and therefore requires special treatment. Several options may exist for the proper handling of the profile at f_{\min} . For example, in [44] the profile at f_{\min} was not used when estimating $\mathcal{F}(\vec{r})$ using (7). In this work, the data at f_{\min} was processed twice. The first time a profile $\mathcal{O}(\vec{r}, \omega_{\min})$ was obtained by using an all-zero initial guess. The second time, the final profile $\mathcal{O}(\vec{r}, \omega_{\min})$ was obtained by using $\beta \mathcal{O}(\vec{r}, \omega_{\min})$ as initial guess. The MF-DBIM approach is summarized in Algorithm 1.

Algorithm 1: The MF-DBIM algorithm

- 1: Set the initial guess $\mathcal{O}^{(0)}$ to an all-zero vector.
- 2: **for** $f = f_{\min}:\Delta f: f_{\max}$ **do**
- 3: Obtain $\mathcal{O}(\vec{r}, 2\pi f)$ with DBIM and $\mathcal{O}^{(0)}$ as initial guess.
- 4: **if** $f = f_{\min}$ **then**
- 5: Set $\mathcal{O}^{(0)} = \beta \mathcal{O}(\vec{r}, 2\pi f_{\min})$.
- 6: Obtain $\mathcal{O}(\vec{r}, 2\pi f)$ with DBIM and $\mathcal{O}^{(0)}$ as initial guess.
- 7: **end if**
- 8: Update $\mathcal{O}^{(0)}$ by median filtering the expression on (10).
- 9: **end for**
- 10: Estimate $\mathcal{F}(\vec{r})$ using (7).
- 11: Estimate $u(\vec{r})$ using (6) and obtain a density image by using $u(\vec{r}) = (\rho_r^{-1/2}(\vec{r}) - 1)$.

III. RESULTS

A. Effects of Imaging Bandwidth and Frequency Separation Δf

The effects of the imaging bandwidth and frequency separation Δf were explored by reconstructing circular cylinders of radii λ , 2λ , and 4λ , where $\lambda = c_0/f_{\max}$ is the wavelength corresponding to the maximum frequency f_{\max} used in the inversion. The speed of sound contrast Δc was normalized using the excess phase $\Delta\phi_{\max}$, i.e., the maximum excess phase that the incident field at frequency f_{\max} accumulates when traveling through the scatterer as opposed to propagating through the background. The magnitude of $\Delta\phi_{\max}$ is commonly used to estimate the region of convergence of single-frequency inverse scattering approaches [45], [46]. All cylinders had $\Delta\phi_{\max} = 0.9\pi$. Density contrast $\Delta\rho$ values of $-\Delta c$ and $-2\Delta c$ were used in the simulations. The synthetic measurements were generated using the analytic scattering solution [47]. The scattered data was corrupted using 2% Gaussian noise, with eight noise realizations per simulation settings. Frequency separation values of $0.01f_{\max}$, $0.05f_{\max}$, and $0.1f_{\max}$ were studied. Also, the use of only two frequencies (i.e., $N_f = 2$) was explored. The reconstruction root mean square error (RMSE) values are shown in Fig. 1.

Although, in general, the use of a lower Δf value resulted in lower reconstruction errors, the quality of the reconstructions depended more strongly on the imaging bandwidth. Furthermore, for most cases the use of two frequencies ($N_f = 2$) resulted in comparable reconstruction errors when compared with the multiple frequency case ($N_f > 2$). The most significant differences when using $N_f = 2$ were observed for low f_{\min}/f_{\max} ratios. Based on this result, $\Delta f = 0.01f_{\max}$ will be used when further exploring MF-DBIM in Sections III-B and III-C unless stated otherwise.

Three algorithmic variations of the MF-DBIM approach were also explored through simulations. The first variation was to use multiple frequency data without frequency hopping. The other two variations are related to the handling of the \mathcal{O} reconstruction at frequency f_{\min} . The second variation consisted of discarding the lowest frequency reconstruction when estimating \mathcal{F}_ρ using (7). The third variation was to process the data at f_{\min} without the reiteration described in Algorithm 1, i.e., eliminating steps 4–7 in Algorithm 1. The imaging target for all cases consisted of a cylinder of radius 4λ with $\Delta\phi = 0.9$ and $\Delta\rho = -\Delta c$. The results are presented in Fig. 2.

The results in Fig. 2(a) demonstrate the importance of using frequency hopping when imaging density using MF-DBIM. In the absence of frequency hopping, the error curves became erratic and the reconstruction errors became large. In particular, the dual-frequency DBIM (DF-DBIM) algorithm [28], [29], [34] corresponds to the limiting case when only two frequencies and no frequency hopping are used, i.e., $N_f = 2$. Further, one can actually

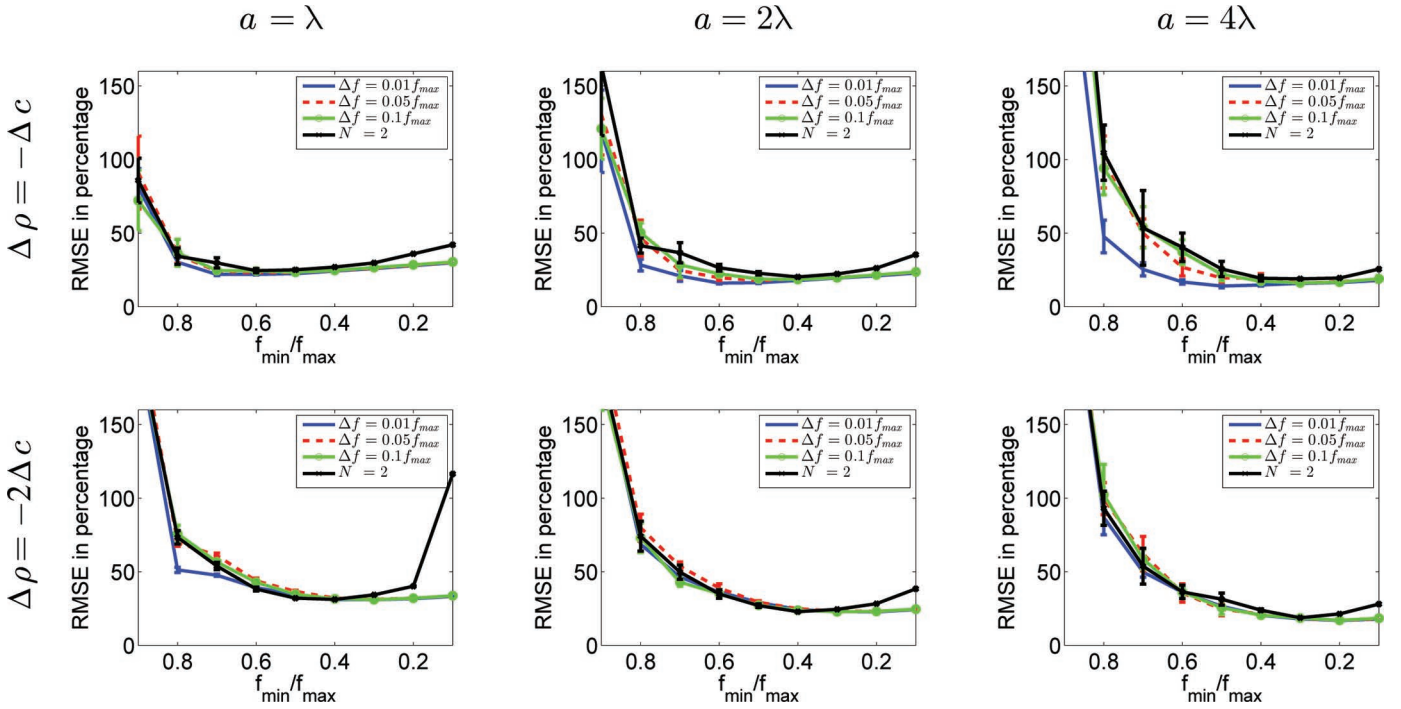


Fig. 1. Effect of Δf on the RMSEs of density reconstructions of λ (first column), 2λ (second column), and 4λ (third column) radius cylinders with $\Delta\rho = -\Delta c$ (top) and $\Delta\rho = -2\Delta c$ (bottom) using MF-DBIM. The SNR was set to 34 dB for all cases.

observe that the reconstruction errors decreased with decreasing number of analysis frequencies for $f_{\min}/f_{\max} < 0.5$. This may be explained by the fact that, in the absence of frequency hopping, the likelihood of incorporating an uncorrelated \mathcal{O} profiles decreases with decreasing number of analysis frequencies.

The results in Figs. 2(b) and 2(c) highlight the importance of properly handling the \mathcal{O} profile obtained at f_{\min} . For the results presented in Fig. 2(b), discarding the profile at f_{\min} effectively increased the minimum analysis frequency to $f_{\min} + \Delta f$. This effect can be negligible when using low Δf values relative to the imaging bandwidth, as in the case of $\Delta f = 0.01 f_{\max}$, but may be significant when large Δf values are used as illustrated by the results obtained with $\Delta f = 0.1 f_{\max}$. However, the most significant effects were observed in Fig. 2(c) where the reconstruction errors had values in excess of 100% for some analysis bandwidths. Although the irregularity of the error curves is similar to that observed in Fig. 2(a), the worst performance was obtained when fewer frequencies were used for estimating \mathcal{F}_ρ for a fixed bandwidth. This is expected because the only partially uncorrelated reconstruction corresponds to f_{\min} independently of the number of analysis frequencies. Therefore, in this case, using more analysis frequencies allowed a reduction in the contribution of this profile to the estimated \mathcal{F}_ρ when using (7).

For further illustration, an example showcasing the performance of the DF-DBIM, the MF-DBIM, and the T-matrix [31] approaches when imaging an inhomogeneous phantom is presented. The comparison with the latter algorithm is presented because of the documented behavioral difference of methods that image density by inverting

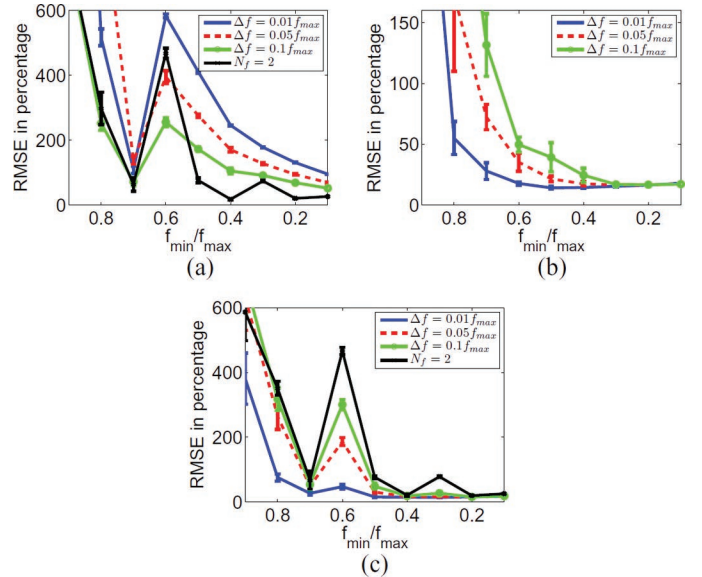


Fig. 2. Algorithmic variations of the MF-DBIM approach. Density images were obtained (a) using multiple frequency information without frequency hopping, (b) discarding the lowest frequency estimate instead of reprocessing the data at f_{\min} , and (c) using lowest frequency estimate without reprocessing. The SNR was set to 34 dB for all cases.

the wave equation for one function at different frequencies (such as DF-DBIM and MF-DBIM) instead of two functions simultaneously (such as the T-matrix approach) [34]. The phantom specifications are given in Table I. An analytical scattering solution was used to calculate the synthetic scattered field [48]. Single-frequency reconstructions were obtained with a termination tolerance of 2% in all cases. The DF-DBIM and MF-DBIM reconstruc-

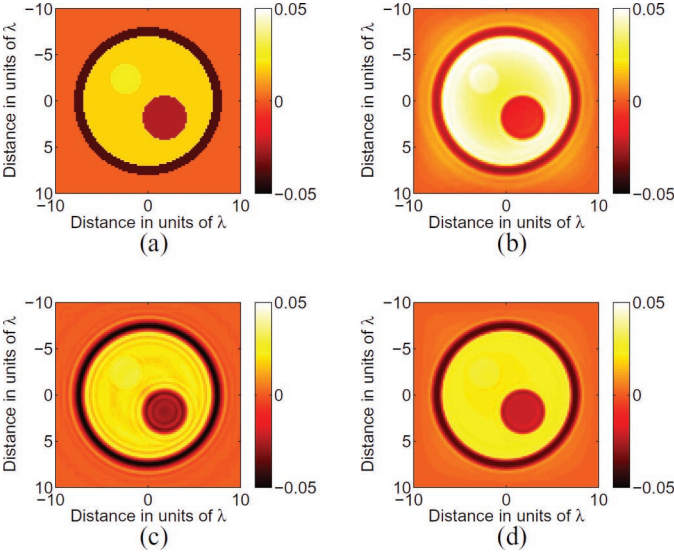


Fig. 3. Density contrast $\Delta\rho$ reconstructions of the computer phantom from Table I using three different algorithms. (a) Ideal density profile. (b) DF-DBIM reconstruction with $f_{\min} = f_{\max}/2$. (c) T-matrix reconstruction with $f_{\min} = f_{\max}/64$. (d) MF-DBIM reconstruction with $f_{\min} = f_{\max}/2$. The $\Delta\rho$ range is limited in all images between -0.05 and 0.05 , and the dimensions are given in terms of the wavelength λ at f_{\max} .

tions were obtained using $f_{\min} = f_{\max}/2$. The T-matrix reconstruction was obtained using $f_{\min} = f_{\max}/64$, which is the minimum bandwidth required for an unbiased density reconstruction using this algorithm given the target size [34], [48]. The reconstructed density images are shown in Fig. 3. The RMSEs in the reconstructions were 90.8%, 33.3%, and 32.4% when using the DF-DBIM, T-matrix, and MF-DBIM approaches, respectively. Although both the MF-DBIM and T-matrix algorithms outperformed the DF-DBIM and provided comparable reconstruction errors, the bandwidth required for convergence of the T-matrix was 32 times larger than that required by the MF-DBIM approach. Therefore, this example illustrates the potential of MF-DBIM to improve upon the convergence characteristics of DF-DBIM while using a significantly smaller bandwidth than the T-matrix approach.

B. Effects of Speed of Sound and Density Contrasts

To more systematically assess the performance of the MF-DBIM approach, circular cylinders of radii λ , 2λ , and 4λ and $\Delta\phi_{\max}$ values of 0.9π , -0.45π , and 0.225π were reconstructed through simulations. The density contrast $\Delta\rho$ of the cylinders was varied between $-3\Delta c$ and $2\Delta c$. The minimum frequency f_{\min} used in the reconstructions was varied between $0.1f_{\max}$ and $0.9f_{\max}$. The synthetic data was contaminated with 2% random Gaussian noise. Five noise realizations per simulation setting were used and the resulting RMSE mean was calculated. The results are presented in Fig. 4. Radial profiles of density reconstructions of cylinders with radius 2λ , $\Delta\phi_{\max} = 0.9\pi$, and $\Delta\rho = -\Delta c$, and $\Delta\rho = \Delta c$ are shown in Fig. 5.

TABLE I. SPECIFICATIONS OF THE COMPUTATIONAL PHANTOM USED FOR DENSITY IMAGING.

Cylinder	Center position	Radius	Δc	$\Delta\rho$
1	[0,0]	8 λ (outer) 7 λ (inner)	4%	-4%
2	[0,0]	7 λ	-1.8%	1.8%
3	[-2.4 λ , 2.4 λ]	1.6 λ	-2.5%	2.5%
4	[1.8 λ , -1.8 λ]	2.4 λ	2.5%	-2.5%

The dimensions are given in terms of the wavelength λ at f_{\max} .

A marked difference in the performance of MF-DBIM was observed when $\Delta\rho/\Delta c > 0$ rather than $\Delta\rho/\Delta c < 0$, i.e., the density and sound speed changes were either in the same direction or in opposite directions. Whereas in the latter case proper convergence (reconstruction RMSEs smaller than 30%) were obtained by using f_{\min} values less than an order of magnitude smaller than f_{\max} , in the former case the errors were significantly larger for comparable magnitudes of $\Delta\rho$ changes. Further, the reconstructions for $\Delta\rho/\Delta c > 0$ became more unstable as $\Delta\phi_{\max}$ increased. The reconstructions in Fig. 5 indicate the main source of error to be the appearance of spurious slopes in regions with ideally homogeneous density.

To further explore this apparent limitation of the MF-DBIM approach to reconstruct certain classes of objects, the object functions $\mathcal{O}(\vec{r})$ corresponding to circular cylinders with radius 2λ , $\Delta\phi_{\max} = 0.9\pi$, and $\Delta\rho = -\Delta c$ and $\Delta\rho = \Delta c$ were obtained using DBIM at frequency f_{\max} . The $\mathcal{F}_\rho(\vec{r})$ profiles were estimated by subtracting the known sound-speed-dependent term from the reconstructed $\mathcal{O}(\vec{r})$ profiles. The ideal profiles for $\mathcal{O}(\vec{r})$ and $\mathcal{F}_\rho(\vec{r})$ were calculated using (3) with the ∇^2 operator implemented using a sinc-based filter. The results are presented in Fig. 6.

The reconstructed $\mathcal{F}_\rho(\vec{r})$ function for the case $\Delta\rho = -\Delta c$ was very consistent with the expected profile, i.e., sharp discontinuities were observed at the edges of the cylinder. In contrast, and although the expected $\mathcal{F}_\rho(\vec{r})$ profile should be almost identical up to a sign change and slight amplitude variation, the $\mathcal{F}_\rho(\vec{r})$ estimate when $\Delta\rho = \Delta c$ appeared completely distorted and exhibited ringing that extended beyond the edges of the imaging target. Given the marked difference in the reconstructed $\mathcal{F}_\rho(\vec{r})$ profiles, the error maps presented in Fig. 4 are expected.

More insight into the nature of the MF-DBIM reconstruction errors can be obtained by analyzing the $\mathcal{O}(\vec{r})$ plots in Fig. 6. The main behavioral difference between the $\Delta\rho = -\Delta c$ and $\Delta\rho = \Delta c$ cases was the smoothness of the ideal $\mathcal{O}(\vec{r})$ functions. For the first case, the destructive interaction between the sound speed and density terms resulted in a smooth $\mathcal{O}(\vec{r})$ function and the DBIM properly converged to an approximate solution that accurately captured density effects. In contrast, the ideal $\mathcal{O}(\vec{r})$ function for the second case exhibited sharp, steep variations that DBIM algorithm had more difficulties reproducing given its limited spectral support [49]. Furthermore, increasing the excess phase $\Delta\phi_{\max}$ made the inverse scatter-

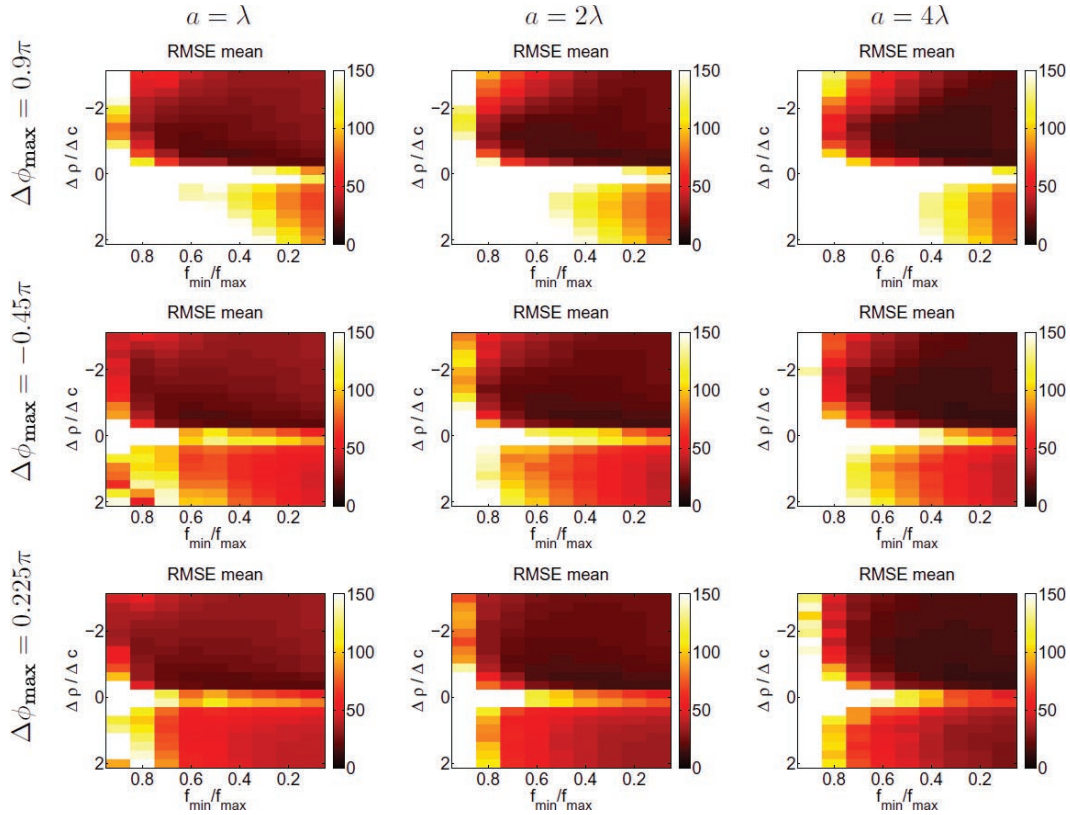


Fig. 4. Mean RMSEs when reconstructing density profiles of homogeneous circular cylinders with $\Delta\phi_{\max} = 0.9\pi$ and radii λ (left), 2λ (center) and 4λ (right) using MF-DBIM. The SNR was set to 34 dB.

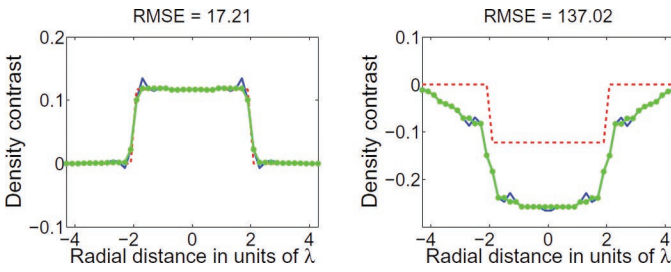


Fig. 5. Reconstructed density profiles of circular cylinders of radius 2λ , $\Delta\phi_{\max} = 0.9\pi$, and $\Delta\rho = -\Delta c$ (left) and $\Delta\rho = \Delta c$ (right) using $f_{\min} = 0.5f_{\max}$.

ing problem more nonlinear and therefore exacerbated the convergence to improper solutions given the lack of sensitivity of the DBIM algorithm to high spatial frequencies.

C. Effects of the Smoothness of the Imaging Target

In the previous section it was observed that objects with smoother $\mathcal{O}(\vec{r})$ profiles were better reconstructed when using the MF-DBIM approach. Further studies of the effect of the smoothness of $\mathcal{O}(\vec{r})$ were conducted by reconstructing cylinders of radii λ , 2λ , and 4λ with sound speed and density profiles smoothed with a radial Hanning function of length equal to λ . The sound speed contrast was set for all cases to obtain $\Delta\phi_{\max} = 0.9\pi$. The results are shown in Fig. 7. Radial profiles of density reconstructions of smooth cylinders with radius 2λ , $\Delta\phi_{\max} = 0.9\pi$, and $\Delta\rho = -\Delta c$ and $\Delta\rho = \Delta c$ are shown in Fig. 8.

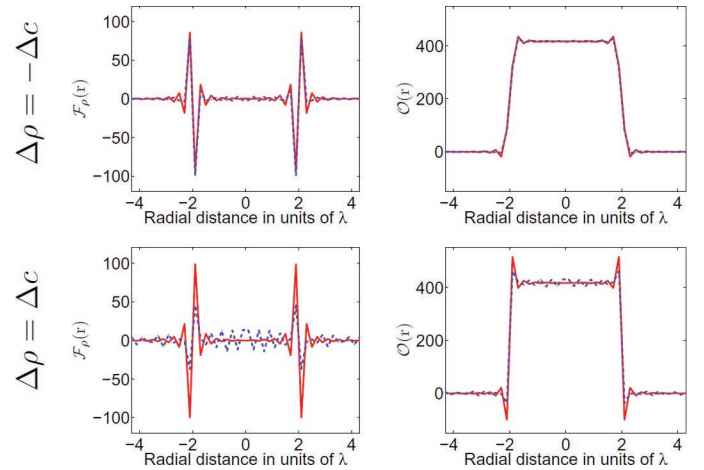


Fig. 6. Expected (solid) and reconstructed (dashed) $\mathcal{F}_\rho(\vec{r})$ (left) and $\mathcal{O}(\vec{r})$ (right) profiles from circular cylinders of radius 2λ , $\Delta\phi_{\max} = 0.9\pi$, and $\Delta\rho = -\Delta c$ (top) and $\Delta\rho = \Delta c$ (bottom).

The smoothness of the imaging targets resulted in more stable inversions than those from the piecewise homogeneous counterparts in Fig. 4. Furthermore, the strong dependence on the sign of $\Delta\rho/\Delta c$ was not observed for the smooth cylindrical targets.

IV. DISCUSSION

The current study presents several contributions to the field of acoustic inverse scattering. An improved algorithm

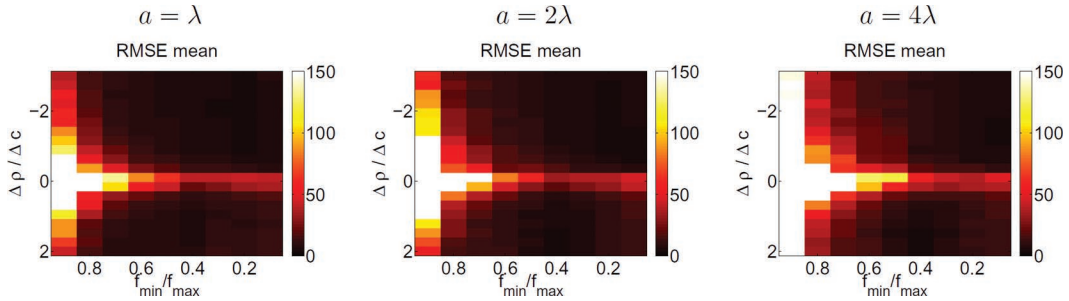


Fig. 7. Mean RMSE when reconstructing density profiles of smooth circular cylinders with $\Delta\phi_{\max} = 0.9\pi$ and radii λ (left), 2λ (center), and 4λ (right) using MF-DBIM. The SNR was set to 34 dB.

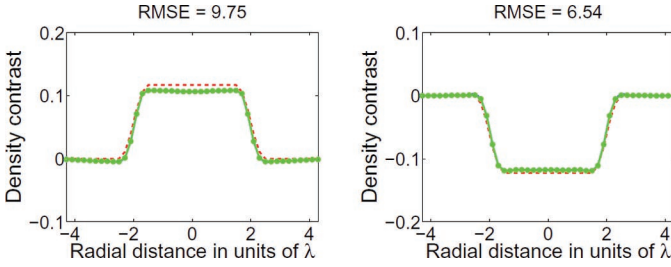


Fig. 8. Reconstructed profiles of smoothed cylinders of radius 2λ , $\Delta\phi_{\max} = 0.9\pi$, and $\Delta\rho = -\Delta c$ (left) and $\Delta\rho = \Delta c$ (right) using $f_{\min} = 0.5f_{\max}$.

(MF-DBIM) was proposed and assessed for constructing tomographic density images. In this study, it was found that MF-DBIM largely overcomes the noise sensitivity issues of its predecessor, the DF-DBIM algorithm, and therefore has the potential to bring density imaging closer to experimental practice.

However, results presented in this study suggest that MF-DBIM has difficulties in reconstructing certain classes of objects. The limiting factor of the technique appears to be related to the high-frequency content of the object function $\mathcal{O}(\vec{r})$ of the imaging target. Scatterers that exhibited smoother $\mathcal{O}(\vec{r})$ profiles were better reconstructed than objects with $\mathcal{O}(\vec{r})$ profiles that exhibited sharp spatial discontinuities. One particular class of objects that resulted in poor density reconstructions were homogeneous cylinders with $\Delta\rho/\Delta c > 0$. Only a few studies have presented density reconstructions from homogeneous cylinders in the past, but all of them presented results corresponding to cylinders with $\Delta\rho/\Delta c < 0$ [31], [32], [34]. This finding may have important implications for practical density tomography given that most healthy tissues exhibit a positive $\Delta\rho/\Delta c$ ratio [18].

Given that all inverse scattering algorithms based on far-field measurements are bandwidth limited, one would expect to observe a degraded performance when using other inverse scattering algorithms to reconstruct density images corresponding to imaging targets with $\mathcal{O}(\vec{r})$ functions that exhibit high spatial frequencies. For illustration, the T-matrix approach [31] was used to create density images corresponding to cylinders with $\Delta\phi_{\max} = 0.9\pi$ and radius 2λ . The RMSEs of the reconstructions for different $\Delta\rho/\Delta c$ values are presented in Fig. 9. The results indi-

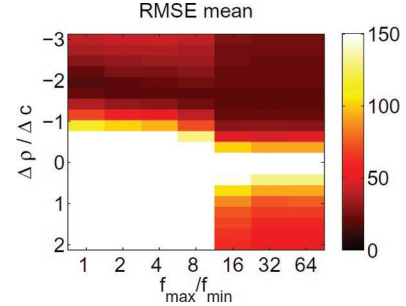


Fig. 9. Mean RMSEs when reconstructing density profiles of homogeneous circular cylinders with $\Delta\phi_{\max} = 0.9\pi$ and radius 2λ using the T-matrix approach. The SNR was set to 34 dB.

cated that the T-matrix approach also has difficulties when imaging homogeneous cylinders with $\Delta\rho/\Delta c > 0$, and therefore supported the hypothesis that the spatial bandwidth of the imaging target impacts the performance of density imaging using inverse scattering.

The results presented in this study indicate the potential of MF-DBIM to handle SNR and bandwidth values that are experimentally obtainable with currently available ultrasound instrumentation [37]. The effects of experimental sources of error, which have been reported to have a significant impact on ultrasonic and microwave tomographic imaging [50]–[52], are yet to be determined. Further, the sensitivity of density imaging methods to the acoustical properties of imaging targets needs to be addressed before techniques such as MF-DBIM can be successfully implemented in practice. MF-DBIM was developed after analyzing the limitations of its simpler counterpart, the DF-DBIM approach [34]. Similarly, understanding the limitations of MF-DBIM should lead to more robust density imaging algorithms. Possible research directions include stabilizing the inversion of (5) by total variation methods [53] which have been proposed in the past for sound speed [54] and density [32], [34] tomographic imaging, and better utilization of the scattered data measurements.

V. CONCLUSIONS

In this work, an improved algorithm (MF-DBIM) for tomographic density imaging was presented and assessed.

The method was capable of obtaining density images with reduced noise sensitivity and total bandwidth when compared with previously available methods reported in the literature. The performance of MF-DBIM degraded when imaging objects that exhibited large spatial frequency variations in their $\mathcal{O}(\vec{r}, \omega)$ profiles. This limitation was related to the limited spatial bandwidth of the inverse scattering problem, and was found to be shared by other tomographic density imaging approaches.

ACKNOWLEDGMENTS

The authors thank Dr. W. D. O'Brien, Jr. for useful discussions on the convergence of density imaging methods.

REFERENCES

- [1] V. G. Murmis, J. J. Gisvold, T. M. Kinter, and J. F. Greenleaf, "Texture analysis of ultrasound B-scans to aid diagnosis of cancerous lesions in the breast," in *IEEE Ultrasonics Symp.*, 1988, pp. 839–842.
- [2] P. M. Shankar, V. A. Dumane, T. George, C. W. Piccoli, J. M. Reid, F. Forsberg, and B. B. Goldberg, "Classification of breast masses in ultrasonic B scans using Nakagami and K distributions," *Phys. Med. Biol.*, vol. 48, no. 14, pp. 2229–2240, Jul. 2003.
- [3] F. L. Lizzi, D. L. King, M. C. Rorke, J. Hui, M. Ostromogilsky, M. M. Yaremko, E. J. Feleppa, and P. Wai, "Comparison of theoretical scattering results and ultrasonic data from clinical liver examinations," *Ultrasound Med. Biol.*, vol. 14, no. 5, pp. 377–385, 1988.
- [4] M. F. Insana, T. J. Hall, and J. L. Fishback, "Identifying acoustic scattering sources in normal renal parenchyma from the anisotropy in acoustic properties," *Ultrasound Med. Biol.*, vol. 17, no. 6, pp. 613–626, 1991.
- [5] M. L. Oelze, W. D. O'Brien Jr., J. P. Blue, and J. F. Zachary, "Differentiation and characterization of rat mammary fibroadenomas and 4T1 mouse carcinomas using quantitative ultrasound imaging," *IEEE Trans. Med. Imaging*, vol. 23, no. 6, pp. 764–771, Jun. 2004.
- [6] K. A. Wear, "Ultrasonic scattering from cancellous bone: A review," *IEEE Trans. Ultrason. Ferroelectr. Freq. Control*, vol. 55, no. 7, pp. 1432–1441, Jul. 2008.
- [7] J. Ophir, I. Cspedes, H. Ponnekanti, Y. Yazdi, and X. Li, "Elastography: A quantitative method for imaging the elasticity of biological tissues," *Ultrasound Imaging*, vol. 13, no. 2, pp. 111–134, Apr. 1991.
- [8] P. E. Barbone and J. C. Bamber, "Quantitative elasticity imaging: What can and cannot be inferred from strain images," *Phys. Med. Biol.*, vol. 47, no. 12, pp. 2147–2164, Jun. 2002.
- [9] J. Bercoff, M. Tanter, and M. Fink, "Supersonic shear imaging: A new technique for soft tissue elasticity mapping," *IEEE Trans. Ultrason. Ferroelectr. Freq. Control*, vol. 51, no. 4, pp. 396–409, Apr. 2004.
- [10] T. Kundu, J.-P. Lee, C. Blase, and J. Bereiter-Hahn, "Acoustic microscope lens modeling and its application in determining biological cell properties from single- and multi-layered cell models," *J. Acoust. Soc. Am.*, vol. 120, no. 3, pp. 1646–1654, Sep. 2006.
- [11] S. Lakshmanan, A. Bodi, and K. Raum, "Assessment of anisotropic tissue elasticity of cortical bone from high-resolution, angular acoustic measurements," *IEEE Trans. Ultrason. Ferroelectr. Freq. Control*, vol. 54, no. 8, pp. 1560–1570, Aug. 2007.
- [12] S. Lakshmanan, A. Bodi, and K. Raum, "Ultrasonic tissue characterization of atherosclerosis by a speed-of-sound microscanning system," *IEEE Trans. Ultrason. Ferroelectr. Freq. Control*, vol. 54, no. 8, pp. 1571–1577, Aug. 2007.
- [13] N. Duric, P. Littrup, A. Babkin, D. Chambers, S. Azevedo, A. Kalinin, R. Pevzner, M. Tokarev, E. Holsapple, O. Rama, and R. Duncan, "Development of ultrasound tomography for breast imaging: Technical assessment," *Med. Phys.*, vol. 32, no. 5, pp. 1375–1386, May 2005.
- [14] J.-W. Jeong, T.-S. Kim, D. C. Shin, S. Do, M. Singh, and V. Z. Marmarelis, "Soft tissue differentiation using multiband signatures of high resolution ultrasonic transmission tomography," *IEEE Trans. Med. Imaging*, vol. 24, no. 3, pp. 399–408, Mar. 2005.
- [15] S. A. Johnson, T. Abbott, R. Bell, M. Berggren, D. Borup, D. Robinson, J. Wiskin, S. Olsen, and B. Hanover, "Noninvasive breast tissue characterization using ultrasound speed and attenuation," in *Acoust. Imaging*, vol. 28, pt. 3, pp. 147–154, 2007.
- [16] S. A. Goss, R. L. Johnston, and F. Dunn, "Comprehensive compilation of empirical ultrasonic properties of mammalian tissues," *J. Acoust. Soc. Am.*, vol. 64, no. 2, pp. 423–457, Aug. 1978.
- [17] S. A. Goss, R. L. Johnston, and F. Dunn, "Compilation of empirical ultrasonic properties of mammalian tissues II," *J. Acoust. Soc. Am.*, vol. 68, no. 1, pp. 93–108, Jul. 1980.
- [18] T. D. Mast, "Empirical relationships between acoustic parameters in human soft tissues," *Acoust. Res. Lett. Online*, vol. 1, no. 2, pp. 37–42, Oct. 2000.
- [19] Y. Saijo, M. Tanaka, H. Okawai, H. Sasaki, S.-I. Nima, and F. Dunn, "Ultrasonic tissue characterization of infarcted myocardium by scanning acoustic microscopy," *Ultrasound Med. Biol.*, vol. 23, no. 1, pp. 77–85, 1997.
- [20] J. N. Yang, A. D. Murphy, E. L. Madsen, J. A. Zagzebski, K. W. Gilchrist, G. R. Frank, M. C. Macdonald, C. A. Millard, A. Faraggi, C. A. Jaramillo, and F. R. Gosset, "A method for in vitro mapping of ultrasonic speed and density in breast tissue," *Ultrasound Imaging*, vol. 13, no. 1, pp. 91–109, Jan. 1991.
- [21] D. K. Nassiri and C. R. Hill, "The use of angular acoustic scattering measurements to estimate structural parameters of human and animal tissues," *J. Acoust. Soc. Am.*, vol. 79, no. 6, pp. 2048–2054, Jun. 1986.
- [22] R. C. Waag, D. Dalecki, and P. E. Christopher, "Spectral power determinations of compressibility and density variations in model media and calf liver using ultrasound," *J. Acoust. Soc. Am.*, vol. 85, no. 1, pp. 423–431, Jan. 1989.
- [23] S. J. Norton, "Generation of separate density and compressibility images in tissue," *Ultrasound Imaging*, vol. 5, no. 3, pp. 240–252, Jul. 1983.
- [24] A. J. Devaney, "Variable density acoustic tomography," *J. Acoust. Soc. Am.*, vol. 78, no. 1, pp. 120–130, Jul. 1985.
- [25] M. Moghaddam and W. Chew, "Variable density linear acoustic inverse problem," *Ultrasound Imaging*, vol. 15, no. 3, pp. 255–266, Jul. 1993.
- [26] S. Mensah and J. P. Lefebvre, "Enhanced compressibility tomography," *IEEE Trans. Ultrason. Ferroelectr. Freq. Control*, vol. 44, no. 6, pp. 1245–1252, Nov. 1997.
- [27] D. Shi and M. A. Anastasio, "Exploitation of symmetries for image reconstruction in linearized variable density diffraction tomography," *J. Acoust. Soc. Am.*, vol. 126, no. 6, pp. 3095–3105, Dec. 2009.
- [28] M. J. Berggren, S. A. Johnson, B. L. Carruth, W. W. Kim, F. Stenger, and P. K. Kuhn, "Ultrasound inverse scattering solutions from transmission and/or reflection data," in *Proc. SPIE*, vol. 671, 1986, pp. 114–121.
- [29] S. Kwon and M. Jeong, "Ultrasound inverse scattering determination of speed of sound, density and absorption," in *IEEE Ultrasonics Symp.*, 1998, pp. 1631–1634.
- [30] M. Moghaddam and W. Chew, "Simultaneous inversion of compressibility and density in the acoustic inverse problem," *Inverse Probl.*, vol. 9, no. 6, pp. 715–730, Dec. 1993.
- [31] J. Lin and W. Chew, "Ultrasonic imaging by local shape function method with CGFFT," *IEEE Trans. Ultrason. Ferroelectr. Freq. Control*, vol. 43, no. 5, pp. 956–969, Sep. 1996.
- [32] K. W. A. van Dongen and W. M. D. Wright, "A full vectorial contrast source inversion scheme for three-dimensional acoustic imaging of both compressibility and density profiles," *J. Acoust. Soc. Am.*, vol. 121, no. 3, pp. 1538–1549, Mar. 2007.
- [33] R. J. Lavarello and M. L. Oelze, "Two approaches for tomographic density imaging using inverse scattering," in *IEEE Ultrasonics Symp.*, 2008, pp. 1298–1301.
- [34] R. Lavarello and M. Oelze, "Density imaging using inverse scattering," *J. Acoust. Soc. Am.*, vol. 125, no. 2, pp. 793–802, Feb. 2009.
- [35] W. C. Chew and Y. M. Wang, "Reconstruction of two-dimensional permittivity distribution using the distorted Born iterative method," *IEEE Trans. Med. Imaging*, vol. 9, no. 2, pp. 218–225, Jun. 1990.
- [36] D. Borup, S. Johnson, W. Kim, and M. Berggren, "Nonperturbative diffraction tomography via Gauss-Newton iteration applied to the

- scattering integral equation," *Ultrason. Imaging*, vol. 14, no. 1, pp. 69–85, Jan. 1992.
- [37] R. J. Lavarello and M. L. Oelze, "A study on the reconstruction of moderate contrast targets using the distorted Born iterative method," *IEEE Trans. Ultrason. Ferroelectr. Freq. Control*, vol. 55, no. 1, pp. 112–124, Jan. 2008.
- [38] P. M. Morse and K. U. Ingard, *Theoretical Acoustics*. Princeton, NJ: McGraw-Hill, 1968.
- [39] S. A. Johnson, F. Stenger, C. Wilcox, J. Ball, and M. J. Berggren, "Wave equations and inverse solutions for soft tissue," in *Acoust. Imaging*, vol. 11, pp. 409–424, 1982.
- [40] S. Pourjavid and O. J. Tretiak, "Numerical solution of the direct scattering problem through the transformed acoustical wave equation," *J. Acoust. Soc. Am.*, vol. 91, no. 2, pp. 639–645, Feb. 1992.
- [41] M. Tracy and S. Johnson, "Inverse scattering solutions by a sinc basis, multiple source, moment method—Part II: Numerical Evaluations," *Ultrason. Imaging*, vol. 5, no. 4, pp. 376–392, Oct. 1983.
- [42] W. C. Chew and J. H. Lin, "A frequency-hopping approach for microwave imaging of large inhomogeneous bodies," *IEEE Microw. Guid. Wave Lett.*, vol. 5, no. 12, pp. 440–441, Dec. 1995.
- [43] O. Haddadin and E. Ebbini, "Imaging strongly scattering media using a multiple frequency distorted Born iterative method," *IEEE Trans. Ultrason. Ferroelectr. Freq. Control*, vol. 45, no. 6, pp. 1485–1496, Nov. 1998.
- [44] R. J. Lavarello and M. L. Oelze, "An improved method for tomographic density imaging using a multiple frequency inverse scattering approach," in *IEEE Ultrasonics Symp.*, 2009, pp. 1467–1470.
- [45] M. Slaney, A. Kak, and L. Larsen, "Limitations of imaging with first-order diffraction tomography," *IEEE Trans. Microw. Theory Tech.*, vol. 32, no. 8, pp. 860–874, Aug. 1984.
- [46] T. Cavicchi, S. Johnson, and W. D. O'Brien Jr., "Application of the sinc basis moment method to the reconstruction of infinite circular cylinders," *IEEE Trans. Ultrason. Ferroelectr. Freq. Control*, vol. 35, no. 1, pp. 22–33, Jan. 1988.
- [47] T. Cavicchi and W. D. O'Brien Jr., "Acoustic scattering of an incident cylindrical wave by an infinite circular cylinder," *IEEE Trans. Ultrason. Ferroelectr. Freq. Control*, vol. 35, no. 1, pp. 78–80, Jan. 1988.
- [48] R. Lavarello and M. Oelze, "Scattering by an arrangement of eccentric cylinders embedded on a coated cylinder with applications to tomographic density imaging," *J. Acoust. Soc. Am.*, vol. 127, no. 2, pp. 645–648, Feb. 2010.
- [49] T. J. Cui, W. C. Chew, X. X. Yin, and W. Hong, "Study of resolution and super resolution in electromagnetic imaging for half-space problems," *IEEE Trans. Antenn. Propag.*, vol. 52, no. 6, pp. 1398–1411, Jun. 2004.
- [50] S. A. Johnson, D. T. Borup, J. W. Wiskin, M. J. Berggren, M. S. Zhdanov, K. Bunch, and R. Eidens, "Application of inverse scattering and other refraction corrected methods to environmental imaging with acoustic or electromagnetic energy," in *Next Generation Environmental Models and Computational Methods*, G. Dolic and M. J. Wheeler, Eds. Philadelphia, PA: SIAM, 1997, pp. 295–312.
- [51] G. L. Wang, W. C. Chew, T. J. Cui, A. A. Aydinler, D. L. Wright, and D. V. Smith, "3D near-to-surface conductivity reconstruction by inversion of VETEM data using the distorted Born iterative method," *Inverse Probl.*, vol. 20, no. 6, pp. 195–216, Dec. 2004.
- [52] R. C. Waag and R. J. Fedewa, "A ring transducer system for medical ultrasound research," *IEEE Trans. Ultrason. Ferroelectr. Freq. Control*, vol. 53, no. 10, pp. 1707–1718, Oct. 2006.
- [53] R. Akar and C. R. Vogel, "Analysis of bounded variation penalty methods for ill-posed problems," *Inverse Probl.*, vol. 10, no. 6, pp. 1217–1229, Dec. 1994.
- [54] C. Li, N. Duric, P. Littrup, and L. Huang, "In vivo breast sound-speed imaging with ultrasound tomography," *Ultrasound Med. Biol.*, vol. 35, no. 10, pp. 1615–1628, Oct. 2009.



Roberto Lavarello was born in Lima, Perú, in 1978. He earned his B.S. degree in electronic engineering in 2000 from the Pontificia Universidad Católica del Perú, Lima, Perú, and his M.S. and Ph.D. degrees in electrical and computer engineering from the University of Illinois at Urbana-Champaign in 2005 and 2009, respectively. Dr. Lavarello is currently a post-doctoral researcher at the University of Illinois at Urbana-Champaign conducting research in ultrasound and is on leave of absence as an assistant professor in the Sección Electricidad y Electrónica at the Pontificia Universidad Católica del Perú. Dr. Lavarello was a Fulbright Scholarship recipient from 2003 to 2005. His research interests include ultrasonic imaging, computational methods for acoustic propagation, quantitative ultrasound, and inverse problems with emphasis on acoustical inverse scattering. He is a member of IEEE and IEEE UFFC.



Michael Oelze was born in Hamilton, New Zealand in 1971. He earned his B.S. degree in physics and mathematics in 1994 from Harding University, Searcy, AR, his M.S. degree in physics in 1996 from the University of Louisiana at Lafayette, Lafayette, LA, and his Ph.D. degree in physics in 2000 from the University of Mississippi, Oxford, MS. Dr. Oelze was a post-doctoral fellow at the University of Illinois at Urbana-Champaign from 2000 to 2004 conducting research in ultrasound. His research interests include the acoustic interaction with soil, ultrasound tissue characterization, quantitative ultrasound, ultrasound bioeffects, ultrasound tomography techniques, ultrasound therapy, and application of coded excitation to ultrasound imaging. Currently, Dr. Oelze is an assistant professor in the Department of Electrical and Computer Engineering at the University of Illinois at Urbana-Champaign. Dr. Oelze is a member of the IEEE, IEEE UFFC, AIUM, and ASA.